Vibration Damping of Thin-Shell Deployable Structures Through Local Buckling

Vibration Damping of Thin-Shell Deployable Structures through Local Buckling

R. Augello[1]* and S. Pellegrino[1]†
[1]*California Institute of Technology, Pasadena, CA, 91125*

This study explores vibration damping induced by local buckling in ultra-thin composite shell structures under frequency-dependent loading. High periodic forces near a resonant frequency can trigger local instabilities, diminishing the shell's ability to transfer loads and strains reducing it dynamic response. Understanding this behavior is essential for optimizing system design. Both experimental and numerical approaches are employed. Experimentally, two boundary conditions are analyzed. Sine sweep loadings are applied to a 500-mm-long Triangular Rollable and Collapsible (TRAC) longeron near its natural torsional frequency at varying amplitudes, with damping ratios determined via the Half-Power Bandwidth Method. Numerically, the structure is modeled using a refined one-dimensional beam finite element based on the Carrera Unified Formulation, with three-dimensional capabilities. Nonlinear dynamics are simulated with an implicit scheme using the Newmark method of the Hilbert-Hughes-Taylor type. Results highlight damping effects caused by local buckling in the flanges of the longeron, as evidenced by variations in damping ratios across the two setups. Simulations closely match experimental results, providing valuable guidance for structural optimization.

Nomenclature

b_l	=	linear differential operator
b_{nl}	=	nonlinear differential operator
$\mathbf{C}$	=	stiffness matrix for linear elastic material
F_τ	=	expansion functions along the thickness coordinate z
$\mathbf{K}_S^{ij\tau s}$	=	fundamental nucleus of the secant stiffness matrix
$\mathbf{K}_T^{ij\tau s}$	=	fundamental nucleus of the tangent stiffness matrix
$\mathbf{L}_{ine}$	=	work of the inertial loads
$\mathbf{L}_{ext}$	=	work of the external loads
$\mathbf{L}_{int}$	=	strain energy
M	=	number of terms in the expansion in the cross-section plane
N_i	=	shape function
N_n	=	number of the finite element nodes per element
$\mathbf{u}_\tau, \mathbf{u}_{\tau i}$	=	generalized displacement vector and finite element nodal parameters
δ	=	variation
$\boldsymbol{\epsilon}$	=	strain vector
$\boldsymbol{\sigma}$	=	stress vector

I. Introduction

Lightweight deployable structures have been developed to address the constraints imposed by the limited payload volume of launch vehicles. With future space missions becoming more demanding research into spacecraft design is shifting towards more capable deployable systems. This shift has prompted the adoption of thin-walled, ultra-thin shell beams with curved cross-sections, valued for their structural simplicity and robustness. A critical aspect of designing these systems lies in understanding their dynamic properties and vibration behavior [1]. To achieve a comprehensive

*Visitor Postdoc, Graduate Aerospace Laboratories, MC 105-50. E-mail: raugello@caltech.edu

†Joyce and Kent Kresa Professor of Aerospace and Civil Engineering; Jet Propulsion Laboratory Senior Research Scientist; Co-Director, Space-Based Solar Power Project, Graduate Aerospace Laboratories, MC 105-50. AIAA Fellow. E-mail: sergiop@caltech.edu

understanding of the structural dynamic behavior of deployable structures, prototypes were created, and vibration experiments were performed alongside modal analyses for different configurations. Wei *et al.* [2] carried out modal analysis and identification for deployable membrane structures. Tan and Pellegrino [3] investigated the nonlinear vibration behavior of cable-stiffened pantographic deployable structures, performing initial broadband modal tests to identify natural frequencies and mode shapes. Wen and Pellegrino [4] examined the frictional shear capacity of a wound roll under launch-induced vibrations. Siriguleng *et al.* [5] studied the vibration modes and modal interactions of a large space-deployable antenna featuring a ring-truss structure.

Due to their lightweight nature and thin-walled design, these structures are susceptible to dynamic excitations, and insufficient damping can result in significant vibration amplification [6]. Under large displacements caused by static loads [7, 8], specific nonlinear local phenomena, such as local buckling, may occur within the structure [9, 10]. This study focuses on analyzing local buckling induced by external cyclic loads and examining its impact on the dynamic behavior of deployable structures.

The deployable structure studied in this work is based on the Triangular Rollable and Collapsible (TRAC) boom architecture, first introduced by Murphey and Banik [11]. It features two tape-spring circular arcs joined along a shared edge, creating a cross-section that enhances bending stiffness and packaging efficiency compared to alternative deployable designs. Longerons with the same cross-sections are utilized in the Caltech Space Solar Power Project (SSPP), which focuses on generating solar energy in space and transmitting it wirelessly to Earth. The SSPP spacecraft is based on a thin-shell composite framework designed to support tensioned membranes embedded with solar cells and RF radiators.[12].

Experimental studies are widely used in the literature for the evaluation of the nonlinear dynamics of deployable structures. Numerical methods are commonly employed to address these problems, as analytical solutions are only applicable to a limited set of cases [13, 14]. The present work employs a finite element formulation based on the Carrera Unified Formulation (CUF) [15] to assess the dynamic behavior and vibration attenuation resulting from local buckling in TRAC longerons. CUF utilizes high-fidelity one-dimensional (1D) finite elements with three-dimensional (3D) capabilities, allowing precise evaluation of cross-sectional deformations through dedicated expansion functions. This approach significantly reduces computational costs by using 1D elements while maintaining accuracy, as no assumptions are required due to the full 3D Green-Lagrange strain tensor being used to derive the nonlinear governing equations [16]. In the context of deployable structures, 1D CUF models have proven highly efficient, particularly in folding analyses of TRAC longerons [17] and their static nonlinear behavior [18]. This study extends the formulation to address nonlinear dynamic problems.

The paper is organized as follows: Section II details the experimental setup and procedures, including the geometric properties and equipment utilized. Section III outlines the numerical model and the CUF formalism, along with the specifics of the Newmark scheme employed for nonlinear dynamic analysis. Sections IV and V present the experimental and numerical results, respectively, with the latter including a comparison of the results of the two approaches. Finally, the main conclusions of the study are presented.

II. Experimental Methods

The TRAC longeron analyzed in this work is shown in Fig. 1. The curved regions of the TRAC are referred to as flanges in this work, whereas the straight region is referred to as the web. Regarding the material properties, the composite layup in the flanges of the longeron is [±45° GFPW / 0° CF / ±45° GFPW], while in the web region, it is [±45° GFPW / 0° CF / $\pm 45_3$° GFPW / 0° CF / ±45° GFPW]. Here, CF represents a thin ply with unidirectional carbon fibers, and GFPW represents a plain weave scrim glass. Both plies are impregnated with resin, as described in [19], and the composite longerons were manufactured in the lab using the methods outlined in [20]. The material properties are reported in Table 1.

	E_1 [GPa]	E_2 [GPa]	G_{12} [GPa]	ν_{12}	t [μm]
CF	128	6.5	7.6	0.35	30
GFPW	23.8	23.8	3.3	0.17	25

Table 1 Material properties of TRAC longeron.

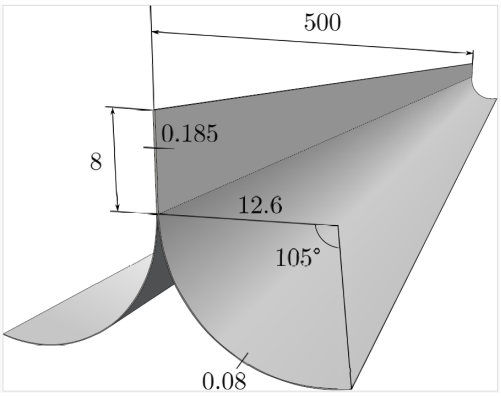

Fig. 1 A longeron analyzed in this paper. The dimensions are expressed in mm.

A. Experimental setup

The longeron is loaded at one end using a Labworks ET-132-203 electrodynamic shaker. The input voltage is provided by the PSV-500 Scanning Vibrometer, a full-field optical vibration measurement system used to determine the velocity at specific points of the longeron. Two boundary conditions are considered for the dynamic analysis:

- Figure 2 illustrates the first setup. The longeron is connected to the shaker at one end and clamped at the other. As

Fig. 2 First set of boundary conditions.

highlighted in Fig. 3, only the web region is clamped, leaving the flanges unconstrained at both ends.

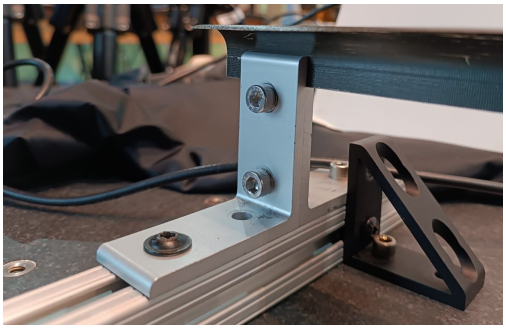

Fig. 3 View of clamped region int the first set of boundary conditions.

- The second setup is shown in Fig. 4. The ends of the longerons were rigidly glued to acrylic plates, preventing the flanges from moving. This setup ensures that the cross-sections at both ends of the longeron are fully constrained. The same sample was analyzed in [8]. The longeron is connected to the shaker at one end and clamped at the other and these details are shown in Fig. 5. Figure 5a specifically illustrates how the left end is clamped using shims The gap between the acrylic plate and the brackets was filled with epoxy resin. As highlighted in [8], the longeron is highly sensitive to initial conditions. Even a small rotation of the end could cause the longeron to buckle. For this reason, the end is rotated by 5°. This approach avoid any buckles in the initial configuration of the longeron.

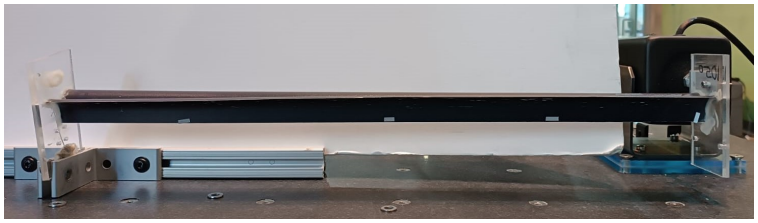

Fig. 4 Second set of boundary conditions.

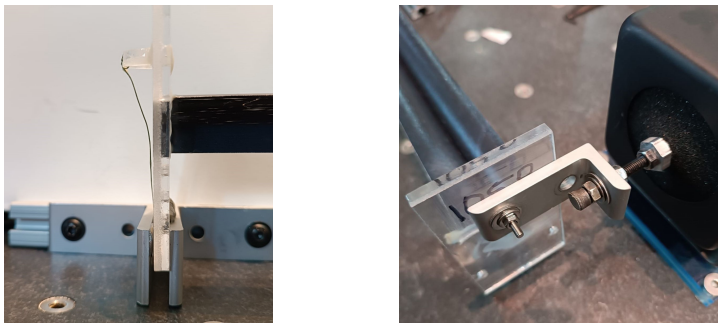

(a) Clamped end **(b) Loaded end**

Fig. 5 Clamped and loaded domains of the second set of boundary conditions.

B. Experimental procedure

As mentioned earlier, a PSV-500 Scanning Vibrometer was used to measure the velocity of the longeron. The experimental procedure is outlined in the following steps.

a The longeron was subjected to a sine sweep input. For the structure under the first boundary condition (see Fig. 2), the sine sweep range from 25 Hz to 40 Hz over 128 seconds. For the second boundary condition (see Fig. 4), the sine sweep range from 75 Hz to 95 Hz over 128 seconds. The frequency range was selected to capture the first natural frequency of the structure.

b The velocity of the output point was measured. The scanned point was located near the free edge of the web at mid-span, as shown in Figs. 2 and 4, where a reflective surface had been placed.

c The velocity vs. time results obtained in step (b) were converted into displacement vs. time data by dividing the velocity distribution by ω values.

d The Hilbert Transform [21] was applied to convert the displacement vs. time distribution into displacement vs. frequency results.

e The process was repeated starting from step (a) for different input amplitudes, and the resulting frequency responses obtained in step (d) were analyzed. The Half-Power Bandwidth Method, a widely used technique for estimating the damping ratio ζ of a vibrating system from its frequency response function was used. This method identifies the bandwidth of the system's response at the points where the amplitude drops by -3 dB (approximately 70.7% of the peak value), corresponding to half of the maximum power. Hence, the damping ratio ζ wass calculated using:

$$\zeta = \frac{\Delta f}{2 f_n} \tag{1}$$

where Δf is the bandwidth representing the range of frequencies where the response amplitude is at least 70.7% of the maximum, and f_n is the resonant frequency.

The evolution of the damping ratio was studied using a Photron FASTCAM high-speed camera to determine whether local buckling occurs in the flanges of the longeron and to identify the amplitude at which buckles form.

III. Numerical model

This section outlines the numerical framework used to develop the mathematical model for simulating the sine sweep experimental tests. The proposed approach combines the Carrera Unified Formulation (CUF) with the Finite

Element Method (FEM). CUF allows for the use of one-dimensional (1D) beam finite elements that can capture any cross-sectional three-dimensional (3D) deformation, through the adoption of arbitrarily selected expansion functions. Notably, the order of the expansion functions is independent of the order of the 1D finite elements, thereby eliminating the aspect-ratio constraints typically imposed by classical FEM approaches. Furthermore, CUF supports any combination of expansion functions, making it suitable for modeling complex cross-sectional geometries, such as TRAC longerons. The present work focuses exclusively on modeling the second set of boundary conditions (see Fig. 4).

A. Refined one-dimensional finite element

The 3D displacement field $u(x, y, z)$ of the longeron of Fig. 1, as well as its variation (denoted by δ), can be expressed as a 2D cross-sectional (x, z) expansion function of the primary unknowns on the axis (y), which are evaluated with FEM. This approach is expressed as:

$$\begin{aligned} \mathbf{u}(x, y, z) &= F_\tau(x, z) N_i(y) \mathbf{u}_{\tau i} \qquad \tau = 1, 2, ..., M \qquad i = 1, 2, \ldots, N_n \\ \delta\mathbf{u}(x, y, z) &= F_s(x, z) N_j(y) \delta\mathbf{u}_{sj} \qquad s = 1, 2, ..., M \qquad j = 1, 2, \ldots, N_n \end{aligned} \tag{2}$$

where $F_\tau(x, z)$ represent the cross-sectional functions depending on the x, z coordinate, $N_i(y)$ stands for the i-th one-dimensional shape function, τ and i are the sum indices, M is the number of terms of the expansion in the cross-section plane, N_n is the number of the FE nodes per element and $\mathbf{u}_{\tau i}$ is the vector of the FE nodal parameters. In this work, quadratic Lagrange polynomials are used for F_τ and classical cubic Finite Elements (FEs) are employed for N_i. Figure 6 shows the detailed application of CUF on the TRAC longeron.

10 cubic 1D finite elements were adopted along the longitudinal direction of the structure, whereas 49 quadratic

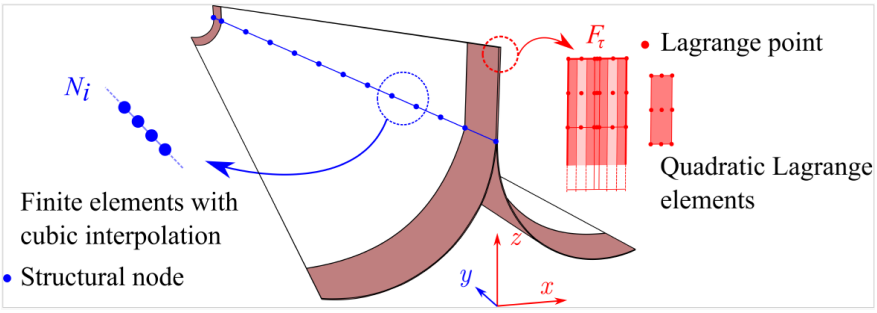

Fig. 6 Numerical model of the TRAC longeron using CUF (red F_τ expansion functions) and FEM (blue N_i shape functions).

Lagrange elements were employed to describe the geometry and the deformation of the cross-section.
In addition, two regions denoted in red in Fig. 6 were added to model the acrylic plates constraining the end sections of the longeron and depicted in Fig. 4. To simulate the high stiffness of the end plates, the material properties shown in Table 1 were scaled by a factor of $\times 10^3$. Linear 1D finite elements were used for the two additional domains. The total number of degrees of freedom was 29997.

B. Nonlinear governing equations

The geometrically nonlinear FE governing equations are obtained according to a total Lagrangian formulation by including all components of the Green–Lagrangian strain tensor. Through the use of the linear and nonlinear differential operators $\mathbf{b}_l$ and $\mathbf{b}_{nl}$ and the stiffness matrix for linear elastic materials, $\mathbf{C}$, the strain–displacement relation, and the constitutive law are

$$\begin{aligned} \boldsymbol{\epsilon} &= \boldsymbol{\epsilon}_l + \boldsymbol{\epsilon}_{nl} = (b_l + b_{nl})\mathbf{u} \\ \boldsymbol{\sigma} &= \mathbf{C}\boldsymbol{\epsilon} \end{aligned} \tag{3}$$

1. Nonlinear dynamics

Using the principle of virtual work the virtual variations of both strain energy δL_{int} and the work done by inertial forces δL_{ine} and external loads δL_{ext} are expressed in CUF formalism:

$$\begin{aligned} \delta L_{int} &= \delta \mathbf{q}_{sj}^T \mathbf{K}_S^{ij\tau s} \mathbf{q}_{\tau i} \\ \delta L_{ine} &= \delta \mathbf{q}_{sj}^T \mathbf{M}^{ij\tau s} \mathbf{q}_{\tau i} \\ \delta L_{ext} &= \delta \mathbf{q}_{sj}^T \mathbf{F}^{sj} \end{aligned} \tag{4}$$

The secant stiffness and mass matrices are denoted as $\mathbf{K}_S^{ij\tau s}$ and $\mathbf{M}^{ij\tau s}$, respectively, while $\mathbf{F}^{sj}$ represents the loading vector. Here, the indices s and j are adopted for the virtual variations of the displacements and have the same bounds as τ and i. The assembled matrices and vectors associated with any arbitrary structural model are constructed by iterating over these four indexes. With this notation, the equations of motion are given by:

$$\mathbf{M}\mathbf{q}(\mathbf{t}) + \mathbf{K}_S(\mathbf{q})\mathbf{q}(\mathbf{t}) = \mathbf{F}(t) \tag{5}$$

The Newton–Raphson method and an implicit step-by-step time integration scheme are used in this work to solve Eq. (5). Omitting the second-order terms and taking into account that the mass matrix is constant, the tangent stiffness matrix deriving from the linearization of the residual nodal forces for a dynamic problem has the following form

$$\begin{aligned} &\delta(\delta L_{int} + \delta L_{ine} - \delta L_{ext}) = \\ &\delta \mathbf{q}_{sj}^T \mathbf{K}_T^{ij\tau s} \mathbf{q}_{\tau i} + \delta \mathbf{q}_{sj}^T \mathbf{M}^{ij\tau s} \mathbf{q}_{\tau i} = 0 \end{aligned} \tag{6}$$

where $\mathbf{K}_T^{ij\tau s}$ is the tangent stiffness matrix. More details of the $\mathbf{K}_T^{ij\tau s}$ matrrix can be found in [22]. Moreover, it should be underlined that the external loads are considered conservative. Therefore, the linearization of the virtual variation of external work is null. The iterative solution adopted in this work is based on the Newmark method, with Hilbert-Hughes-Taylor algorithm [23]. Interested readers are referred to [24] for the derivation of the Newmark method in CUF formalism.

2. Nonlinear static

For the nonlinear static analysis, the principle of virtual work can be written as

$$\delta L_{\text{int}} = \delta L_{\text{ext}} \tag{7}$$

Introducing Eqs. (4) into (7), and looping on indexes τ and i, the following nonlinear equation holds

$$\mathbf{K}_S\ \mathbf{q} = \mathbf{F} \tag{8}$$

Equation (8) represents a geometrically nonlinear systems, and it is tipically computed adopting a linearization technique. In this paper, the employed linearization technique is the Newton-Raphson method, along with a displacement control algorithm. The details of the derivation can be found in [25].

3. Nonlinear modal analysis

The nonlinear modal analysis starts from Eq. (6). Neglecting the external forces and assuming harmonic displacements, the equations of motion for free vibrations hold the form of a classical eigenvalue problem, which in unified form reads:

$$(\mathbf{K}_T^{ij\tau s} - \omega^2 \mathbf{M}^{ij\tau s})\mathbf{q}_{\tau i} = 0 \tag{9}$$

where ω is a natural period and $\mathbf{q}_{\tau i}$ the related amplitude eigenvector. The accuracy of the proposed methodology relies heavily on the structural theory's ability to accurately capture nonlinear behavior, a capability well demonstrated by the current CUF methodology. Since the nonlinear vibrations of the longeron begins lower amplitudes, the linearization around specific points along the equilibrium path, combined with the assumption of harmonic oscillations, is considered valid. Furthermore, the inertial effects are neglected when determining the equilibrium path thus, simplifying the analysis. In essence, the vibrations are analyzed as deviations around quasi-static equilibrium states, ensuring a robust and efficient approach to modeling the system's dynamic behavior. This approach has already been validated in [26].

IV. Experimental Results

This section presents the main experimental results obtained for both boundary conditions. For each condition, the following steps are followed:

a The measured displacement vs. frequency responses are plotted for increasing amplitude levels, up to the maximum value for which the vibrometer can accurately measure velocity.

b The non-dimensional displacement (normalized by the input displacement) vs. frequency is plotted. This graph provides initial insights into the evolution of the damping ratio.

c A high-speed camera is used to visually inspect whether local buckling is occurring;

d The evolution of the damping ratio is evaluated for each input amplitude.

Finally, the two sets of results are compared to assess the effect of local buckling on the dynamic response of the TRAC longeron.

A. First boundary condition

The longeron in Fig. 2 was subjected to a sine sweep ranging from 25 to 40 Hz. The input varied from 10 to 400 mV, which represents the upper limit for which the vibrometer can measure results. The actual transverse displacement results are shown in Fig. 7.

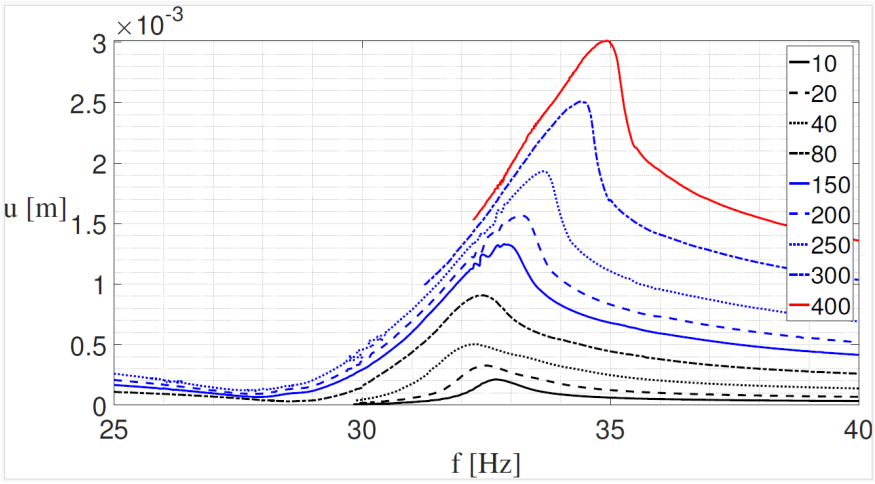

Fig. 7 Transverse displacement vs. frequency response of the longeron shown in Fig. 2. Each curve represents a different input amplitude, as indicated in the legend (in mV).

A typical backbone curve, characteristic of a nonlinear dynamical system, is clearly evident. As a result, the natural frequency shifts from 32.6 Hz with an input of 10 mV to 34.9 Hz with an input of 400 mV. The highest recorded displacement is 3 mm. The same results are presented in a non-dimensional form in Fig. 8, where the actual displacement is normalized by the input displacement (as measured by the vibrometer).

This figure clearly illustrates the evolution of damping caused by the inherent nonlinearity present in the system. Two distinct behaviors can be observed: initially, for input levels ranging from 10 to 80 mV, a softening behavior is evident, leading to a slight decrease in the natural frequency. In this domain, the system's stiffness appears to reduce as the input increases, which is characteristic of a softening nonlinear response. Subsequently, as the input from 80 mV to 400 mV, the natural frequency begins to increase, indicating a transition to a different regime of behavior. Throughout these observations, the damping coefficient is seen to monotonically increase as the amplitude of the external input grows. This implies that the energy dissipation in the system becomes more significant with higher excitation levels, which is consistent with the expected effects of increased nonlinearities in the structure.

To further investigate the potential occurrence of localized instabilities, a high-speed camera was employed to visually examine whether local buckling takes place under the highest loading conditions. Figure 9 provides three snapshots taken at the maximum input amplitude of 400 mV. These images correspond to peaks of the frequency response, where the structure is subjected to its highest level of dynamic excitation.

It is evident that no local buckling occurs within the flanges. Consequently, the influence of local buckling on the dynamic response of the longeron cannot be assessed solely through the results of this experiment. The absence of

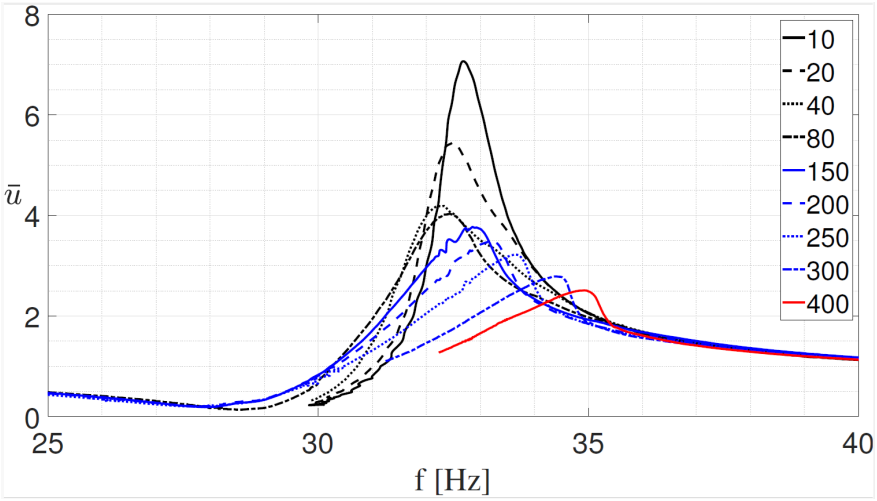

Fig. 8 Non-dimensional displacement (normalized by input displacement) vs. frequency response of longeron. Each curve represents a different input amplitude, as specified in the legend (in mV).

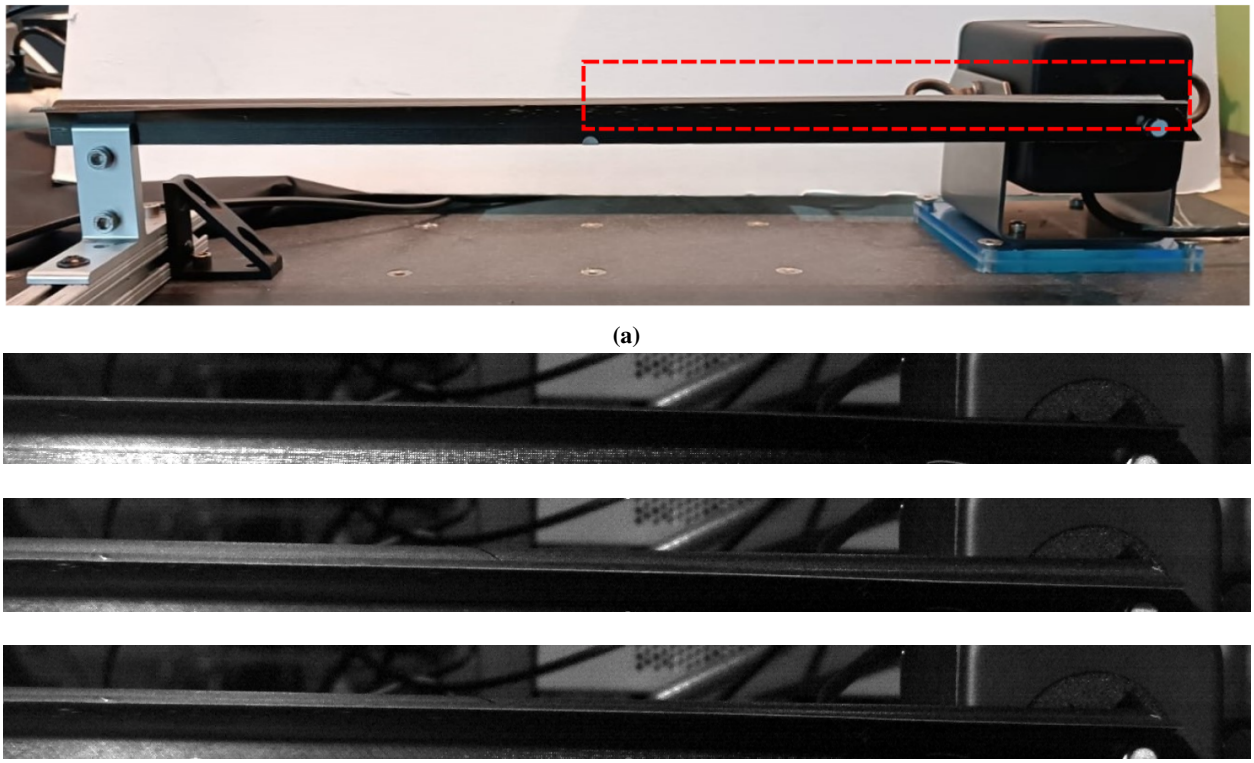

(a)

Fig. 9 Snapshots of longeron shown in Fig. 2 in the domain highlighted in (a), taken at the peak of the frequency response for an excitation amplitude of 400 mV.

visible buckling suggests that either the current loading conditions are insufficient to induce local instabilities or that the longeron boundary conditions are inherently resistant to such effects at the tested amplitudes.
Finally, the evolution of the damping ratio as a function of the input amplitude is presented in Fig. 10.

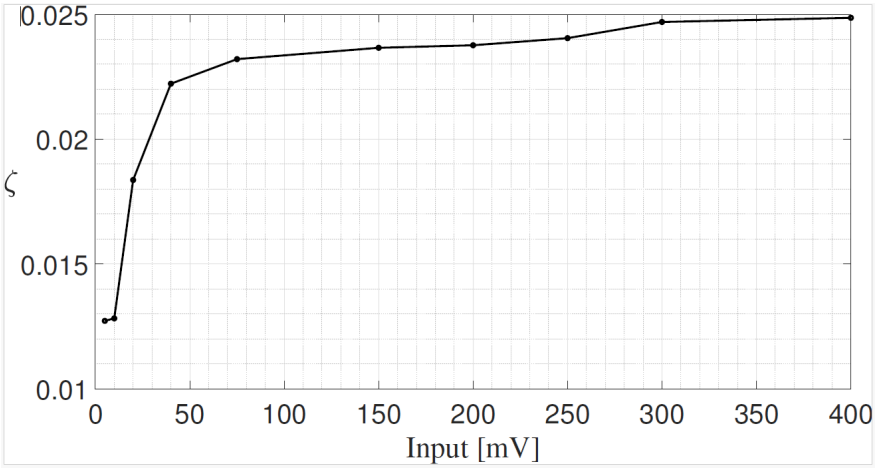

Fig. 10 Damping ratio evolution of longeron shown in Fig. 2.

This figure shows that after a initial region where the damping ratio remains practically constant, it begins to increase noticeably. From 10 to 80 mV, the damping ratio experiences a rapid rise, which corresponds to a softening behavior of the structure (see Fig. 8). This excitation range is characterized by a decrease in stiffness, indicating greater energy dissipation as the input amplitude increases. Following this rapid increase, the damping ratio reaches a plateau, where it stabilizes despite further increases in input. This plateau, occurring between 80 and 400 mV, corresponds to a hardening behavior of the structure. In this region, the structural response begins to stiffen, reducing the rate of energy dissipation growth.

B. Second boundary condition

Since the previous boundary conditions did not reveal any evidence of local buckling, a second set of boundary conditions was applied, providing stiffer ends that constrain both the web and the flanges, as shown in Fig. 4. This configuration aims to increase the structural rigidity and potentially elicit different dynamic behavior under similar loading conditions. The transverse displacement vs. frequency response is shown in Fig. 11. In this case, the input amplitude ranges from 10 to 250 mV, with the highest recorded displacement reaching 0.85 mm.
A softening behavior is observed, indicated by a slight decrease in natural frequency from 88.85 Hz at an input of 10 mV to 87.57 Hz at 250 mV. Although this change in frequency is relatively minor, it highlights the influence of increased input amplitude on the stiffness characteristics of the system. The non-dimensional displacement distributions are presented in Fig. 12.
Similar to the previous boundary conditions, the damping ratio exhibits a consistently increasing trend across the range of input amplitudes. However, unlike the earlier case, there is no evidence of stiffening behavior as the input amplitude increases. This suggests that while energy dissipation continues to grow, the system does not exhibit the same nonlinear hardening effects, possibly due to differences in constraint conditions. To further understand the structural response, particularly the potential onset of local buckling in the flanges, high-speed cameras were utilized to capture the behavior under dynamic loading. The most significant snapshots, taken at input levels of 10, 100, and 180 mV, are presented in Fig. 13.
While no local buckling is evident for input levels of 50 and 100 mV, a local buckle appears at 180 mV. This local instability occurs near the mid-span of the longeron, indicating a point where the structure's resistance to compressive forces becomes insufficient under increased dynamic loading. The onset of buckling is marked by a visible deformation that was not present at lower input amplitudes. Moreover, Fig. 14 shows a second local buckle close to the loaded end. The figure shows that localized buckling occurrs at the peak value in the position corresponding to the opposite phase of the buckling depicted in the Fig. 13c.
Finally, the evolution of the damping ratio is presented in Fig. 15. Notably, buckling of the flanges is observed at a

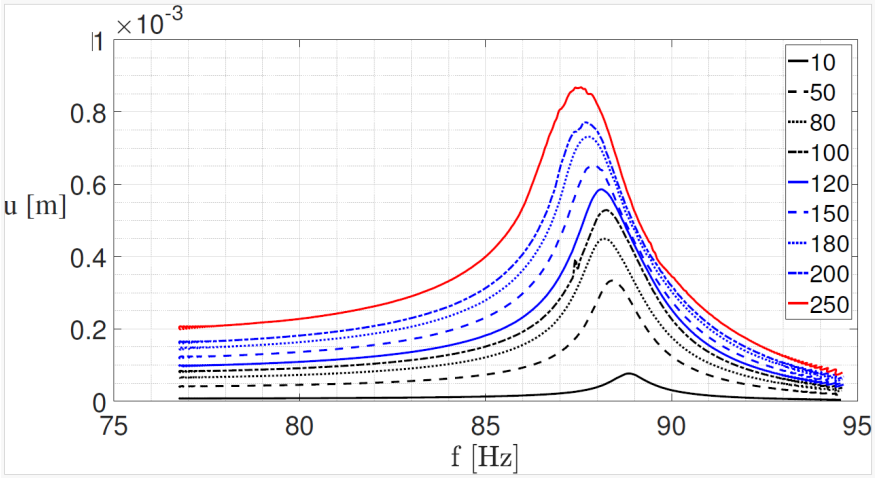

Fig. 11 Transverse displacement vs. frequency response of longeron shown in Fig. 4. Each curve represents a different input amplitude, as indicated in the legend (in mV).

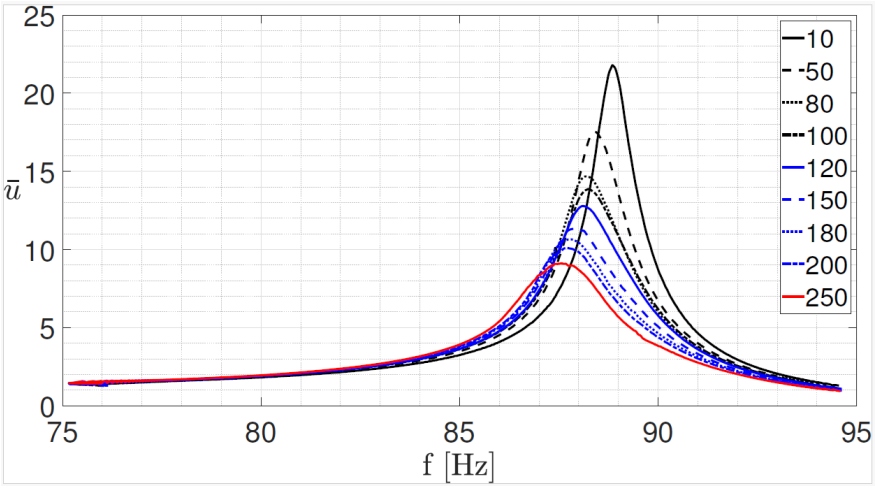

Fig. 12 Non-dimensional displacement (normalized by input displacement) vs. frequency response of longeron shown in Fig. 4. Each curve represents a different input amplitude, as specified in the legend (in mV).

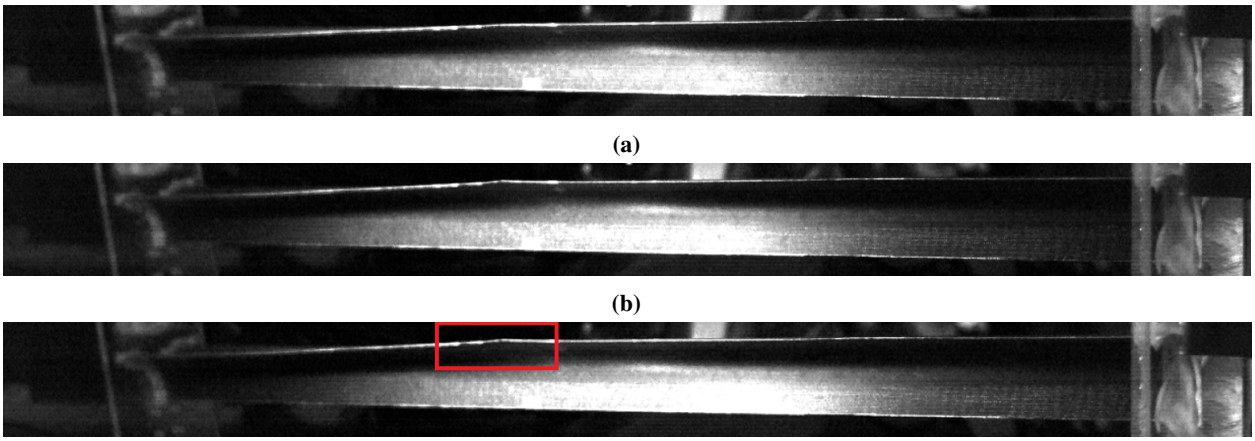

(a)

(b)

(c)

Fig. 13 Snapshots of longeron in Fig. 4, taken at the peak of the frequency response for an excitation amplitude of 50 (a), 100 (b) and 180 (c) mV.

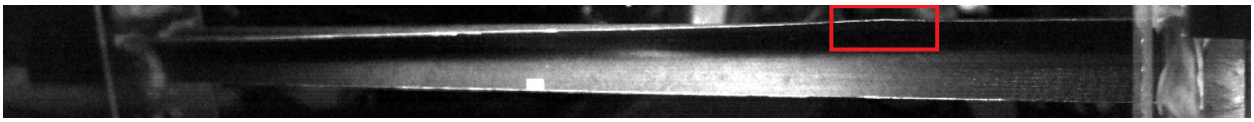

Fig. 14 Snapshot of longeron in Fig. 4, taken at the peak of the frequency response for an excitation amplitude of 180 mV. Local buckling occurring near the loaded region.

damping ratio corresponding to an excitation voltage of 180 mV. At this voltage level, the damping ratio is approximately 0.01, suggesting that there is a critical threshold above which structural instabilities become apparent.

C. Comparison of Experimental Results

A comparative analysis of the progression of the damping ratio under the second boundary condition with the results depicted in Fig. 10 is presented in Fig. 16. It reveals several common characteristics, summarized as follows, according to the colored areas of Fig. 16:

- **Yellow**: In the initial region of low input voltage amplitudes (up to 10 mV), the damping ratio exhibits a constant behavior, consistent with the observations under the first boundary condition;
- **Red**: Between 10 mV and 90 mV, the damping ratio shows a steep rise from 0.005 to 0.009. This behavior mirrors the trend identified for the first boundary condition, where the damping ratio increases from 0.013 to 0.023 over a similar range of input voltages (10 mV to 75 mV).
- **Cyan**: A subsequent plateau-like phase is observed, characterized by a slower increase in the damping ratio, from 0.009 to 0.01 as the input voltage ranges between 90 mV and 180 mV. This behavior aligns with the trend identified in Fig. 10, where the damping ratio rises modestly from 0.023 to 0.025 over an extended voltage range (75 mV to 400 mV).
- **Green**: Beyond 180 mV, the damping ratio under the second boundary condition exhibits a marked increase, surpassing the plateau phase. The growth rate is notably higher than in the previous domains, with the damping ratio increasing from 0.01 to 0.019 as the input voltage spans 180 mV to 340 mV. This transition coincides with the emergence of localized buckling, as verified through high-speed camera investigations.

The behavior described in the final excitation range highlights a damping effect directly associated with the onset of local buckling in the flanges of the TRAC longeron.

V. Numerical Results

The numerical results presented in this study were obtained by replicating the experimental test under the second set of boundary conditions illustrated in Fig. 4. Initially, an assessment of the model's performance was conducted by

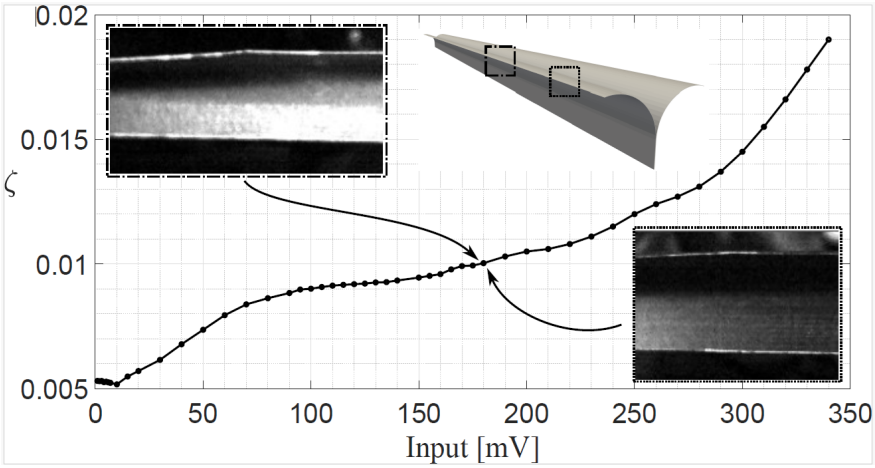

Fig. 15 Damping ratio evolution of longeron shown in Fig. 4.

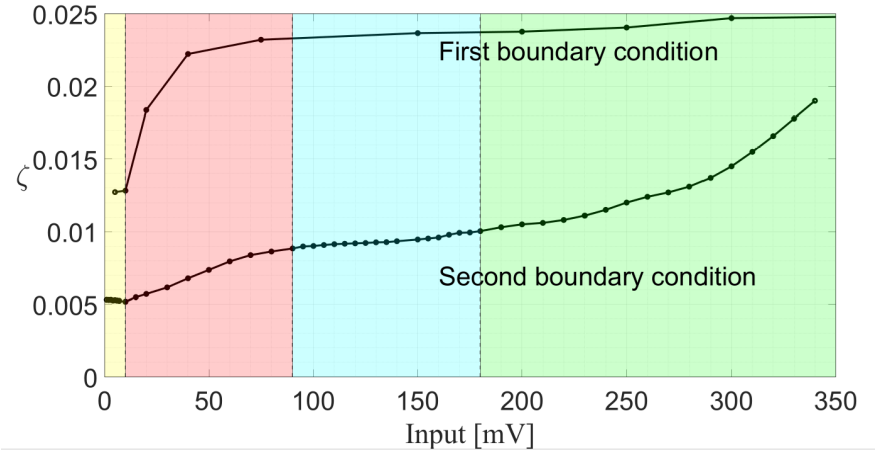

Fig. 16 Comparison of the damping ratio evolutions in Figs. 10 and 15.

comparing its results with those of the experimental test for both static and modal analyses. Subsequently, a nonlinear dynamic analysis was performed by subjecting the structure to the same external loadings used in the experimental setup.

A. Assessment of the model

1. Nonlinear static

A nonlinear static analysis was conducted on the structure by applying a rotation to the unloaded end. In this analysis, no excitation was imposed by the shaker, and the structure was rotated at the other end. As detailed in Section II.A, this approach was employed to prevent the onset of local buckling. The test was initially performed with a torsional rotation of 5°, a value chosen to avoid static local buckling. However, when the rotation was increased to 8°, local buckling became evident. The corresponding results are presented in Fig. 17a, clearly showing local buckling of the front flange.

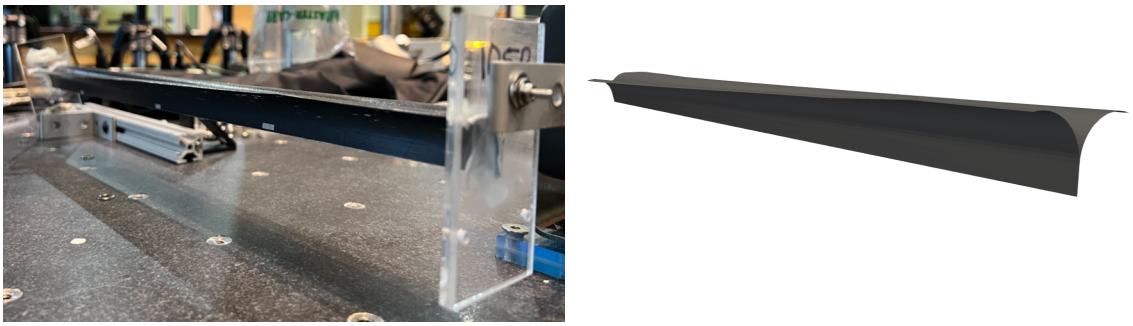

(a) **(b)**

Fig. 17 Experimental (a) and numerical (b) results for a torsional rotation of the unloaded end of 8°. No external excitations is applied and the end attached to the shaker is fully clamped in the numerical simulations.

The numerical model was subjected to the same rotation, with the end attached to the shaker fully clamped. As shown in Fig. 17b, the model successfully replicates the buckling observed in the experiment, offering valuable evidence of its validity and reliability.

2. Modal analysis

Subsequently, a modal analysis was performed on the structure to evaluate its dynamic characteristics. Initially, the analysis focused on the unloaded configuration, where both ends of the structure are fully clamped to simulate fixed boundary conditions. In this setup, the first natural frequency was determined to be 98.17 Hz, corresponding to a torsional mode shape. This result provides critical insights into the structural response and serves as a benchmark for comparison with other configurations or loading conditions. The torsional mode shape and the associated frequency are illustrated in Fig. 18. Then, the modal shape and the associated natural frequency were evaluated for longeron with the

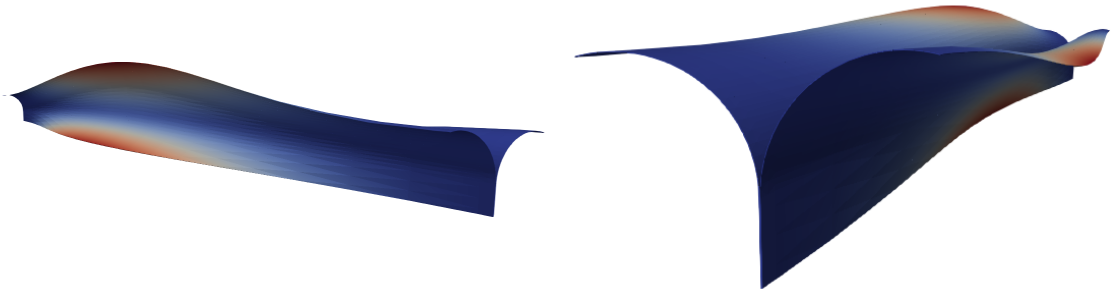

Fig. 18 Torsional mode shape of undeformed longeron with both ends fully clamped. Natural frequency: 98.17 Hz.

end rotated by 5°, as in the experiment. The results are shown in Fig. 19

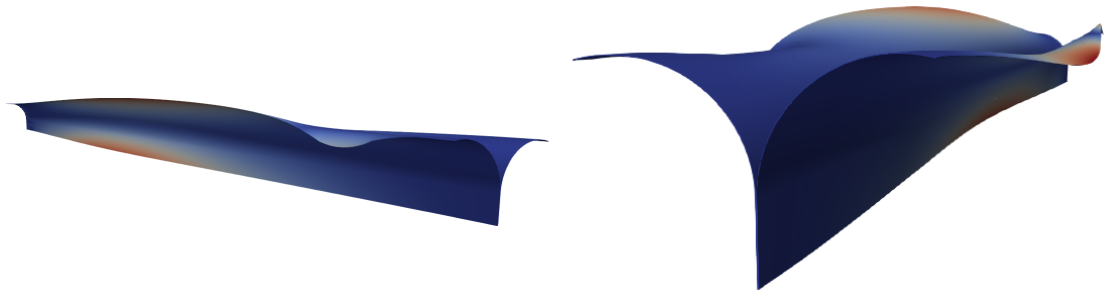

(a) Clamped end **(b) Loaded end**

Fig. 19 Torsional mode shape of longeron with the end rotated by 5°. Natural frequency: 89.16 Hz.

For the unloaded configuration, the first natural frequency corresponds to the torsional mode shape. Notably, this frequency decreases from 98.17 Hz to 89.16 Hz due to a reduction in local stiffness, particularly in specific regions of the structure. This stiffness decrease is most pronounced near the front flange close to the end connected to the excitation source. The same phenomenon is observed dynamically, as captured by the high-speed camera, with results shown in Fig. 14. Finally, a detailed comparison of the numerical natural frequencies and those obtained experimentally is presented in Table 2, highlighting the accuracy and consistency of the numerical model in replicating the experimental findings. The natural frequency derived from the experimental results is obtained from Fig. 12. For the lowest input

	Numerical Model		Experiment
	Undeformed	Deformed	10 mV
f_n	98.17	89.16	88.85

Table 2 Material properties of TRAC longeron.

analyzed, corresponding to 10 mV, the natural frequency was measured as 88.85 Hz. This value is in close agreement with the natural frequency calculated for the deformed configuration in the numerical model. The percentage difference between the two values is just 0.35%, demonstrating excellent correlation between the experimental and numerical results.

B. Nonlinear dynamics

The nonlinear dynamic analyses performed on the numerical model were carried out using input voltage levels from 5 mV to 250 mV. These specific voltage values were chosen to investigate the system's behavior across a range of excitation intensities, ensuring that both low-amplitude and high-amplitude responses were captured. The results of these analyses are presented as frequency response curves, depicting the actual displacements of the system under the specified input conditions in Fig. 20.

C. Comparison of Experimental and Numerical Results

The results, when compared to those presented in Fig. 11, lead to several interesting observations:

- The peak displacements of the simulated longeron closely match those observed experimentally data for each amplitude level under consideration. This alignment underscores the model's ability to replicate the system's global response characteristics effectively, in terms of maximum displacements;
- A notable difference emerges when comparing the frequency response trends. In the numerical simulations, the frequency increases as the input amplitude rises from 5 mV to 250 mV. Conversely, the experimental data reveal a decrease in the natural frequency with increasing input amplitude. This discrepancy arises from the fact that the numerical model does not incorporate structural damping, which has been neglected in the proposed framework;

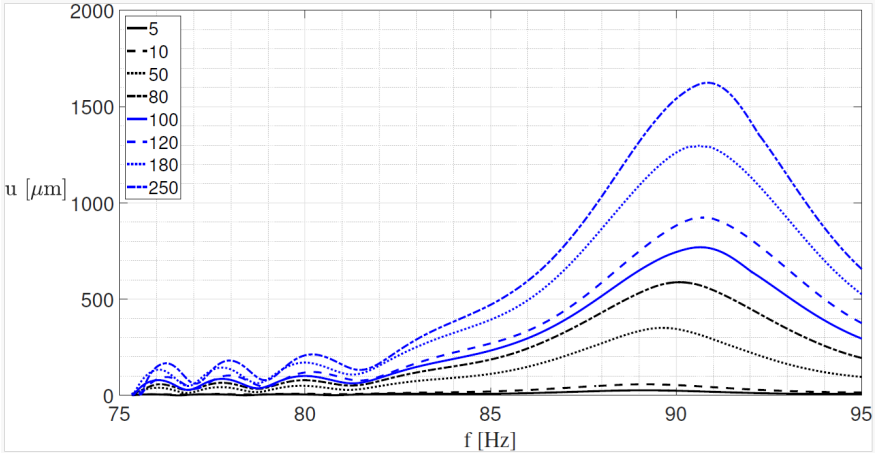

Fig. 20 Transverse displacement vs. frequency response obtained from the numerical model of the longeron. Each curve represents a different input amplitude, as indicated in the legend (in mV).

- The absence of damping in the numerical simulation is further validated by the behavior of the non-dimensional curves presented in Fig. 21:
  - a The curves corresponding to 5 mV and 10 mV exhibit close peak levels, confirming a linear structural response. This linearity is further supported by Fig. 15, which demonstrates a constant damping ratio in this amplitude range;
  - b In this range, the peak non-dimensional displacement increases, contrary to the numerical results where it decreases. This discrepancy arises from the absence of damping in the numerical simulation. The observed increase is dominated by the structural nonlinearity resulting from large displacements;
  - c Between 120 mV and 250 mV, a reduction in peak amplitude is observed, indicating the activation of damping effects due to local buckling. Examining the deformed shapes of the structure at input levels of 120 mV and 200 mV shown in Figs, 22 and 23 reveals a critical insight. At 200 mV, the flanges exhibit clear signs of local buckling, indicating the system's transition into a nonlinear deformation regime. This phenomenon, absent at 120 mV, marks a significant threshold in the structural behavior under high excitation amplitudes. The buckling of the flanges is evident and is indicative of the limits of the structure's stability in this configuration.

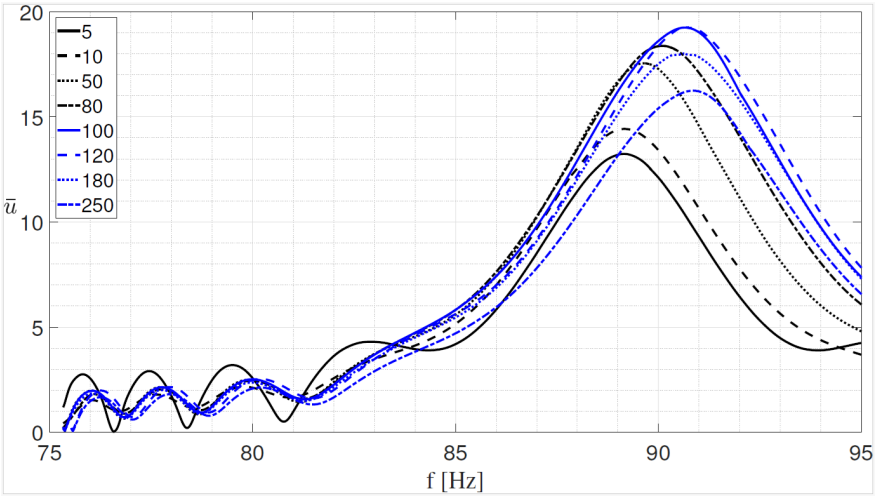

Fig. 21 Non-dimensional displacement (normalized by input displacement) vs. frequency response of the numerical model of the longeron. Each curve represents a different input amplitude, as indicated in the legend (in mV).

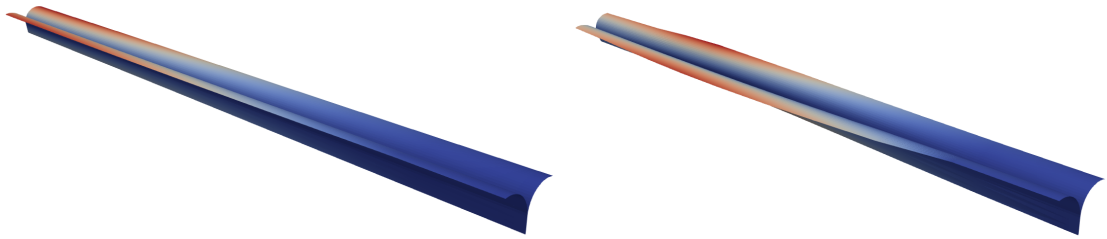

(a) (b)

Fig. 22 Deformed configuration under 120 mV (a) and 200 mV (b) input amplitudes. Positive displacement.

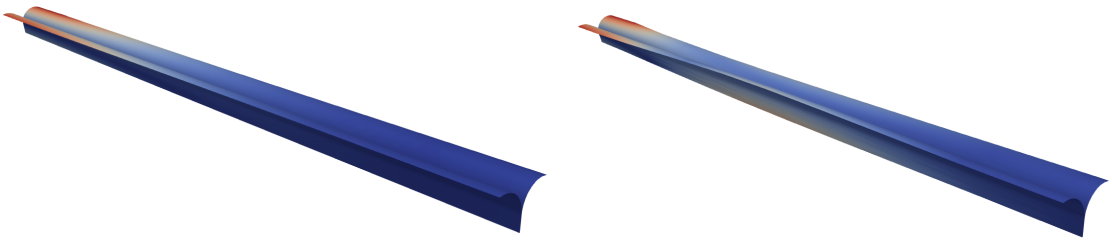

(a) (b)

Fig. 23 Deformed configuration under 120 mV (a) and 200 mV (b) input amplitudes. Negative displacement.

The local buckling observed in Fig. 22b closely matches the experimental results shown in Fig. 14, indicating strong agreement between the numerical model and the physical tests for this specific case. However, the local buckling depicted in Fig. 23b differs from the experimental findings presented in Fig. 13c. In the numerical simulations, local buckling is detected near the clamped end on the back flange. Conversely, in the experimental setup, the buckling occurs at the center of the front flange. The difference likely arises due to the lack of initial perturbations or imperfections in the numerical model, which are present in the physical system and significantly influence the buckling pattern.

VI. Conclusion

The impact of local buckling on the dynamic behavior of TRAC longerons has been studied through experimental tests. Two boundary conditions have been considered, and sine sweep tests with progressively increasing amplitudes have been conducted, calculating the damping ratio using the Half-Power Bandwidth Method. In the first configuration, the TRAC was clamped only at the web, leaving the flanges unconstrained, while the opposite end is excited using a shaker. Since the flanges were free, no compressive forces develop, and high-speed camera observations confirm the absence of local buckling. In the second configuration, both ends, including the flanges and the web, were clamped. In this setup, buckling occurred at higher amplitude levels, accompanied by a noticeable increase in the damping ratio. This phenomenon, absent in the first setup, highlights the role of local buckling in enhancing damping and its influence on the dynamic response of the deployable structure.

The analyses were also performed using a numerical model based on the Carrera Unified Formulation (CUF). This approach enables the creation of refined one-dimensional finite elements, significantly reducing computational costs compared to traditional two-dimensional or three-dimensional finite element methods. CUF can accurately capture three-dimensional deformations through expansion functions, effectively representing the complex geometry of the TRAC longeron. Nonlinear dynamic analyses were conducted with this model using the Newmark algorithm combined with the Hilbert-Hughes-Taylor method, applying highest numerical damping to ensure convergence. The numerical results were compared to those from the second experimental configuration, showing strong agreement in both frequency response curves and the evolution of the damping ratio.

Future work will address the discrepancy between the local buckling detected by the numerical model and shown in Fig. 23b and the one from experiment in Fig. 13c. To address this discrepancy, an initial geometric perturbation can be introduced into the numerical model. This perturbation would mimic the inherent imperfections of the experimental

setup, such as slight deviations in geometry, material inconsistencies, or residual stresses, which tend to dictate the location and shape of buckling. By incorporating these imperfections, the numerical model would be better equipped to replicate the experimental buckling behavior.

Acknowledgments

This research was carried out with financial support from the Caltech Space Solar Power Project and it is part of the project NOVITAS, funded by the European Union's Horizon Europe research and innovation program under the Marie Sklodowska-Curie grant agreement No 101059825.

References

[1] Zhang, X., Nie, R., Chen, Y., and He, B., "Deployable structures: structural design and static/dynamic analysis," *Journal of Elasticity*, 2021, pp. 1–37.

[2] Wei, J., Ma, R., Liu, Y., Yu, J., Eriksson, A., and Tan, H., "Modal analysis and identification of deployable membrane structures," *Acta Astronautica*, Vol. 152, 2018, pp. 811–822.

[3] Tan, G., and Pellegrino, S., "Nonlinear vibration of cable-stiffened pantographic deployable structures," *Journal of Sound and Vibration*, Vol. 314, No. 3-5, 2008, pp. 783–802.

[4] Wen, A., and Pellegrino, S., "Launch Vibration of Pre-Tensioned Coiled Structures," *AIAA SCITECH 2022 Forum*, 2022, p. 1883.

[5] Siriguleng, B., Zhang, W., Liu, T., and Liu, Y., "Vibration modal experiments and modal interactions of a large space deployable antenna with carbon fiber material and ring-truss structure," *Engineering Structures*, Vol. 207, 2020, p. 109932.

[6] Pappa, R. S., Lassiter, J. O., and Ross, B. P., "Structural dynamics experimental activities in ultralightweight and inflatable space structures," *Journal of Spacecraft and Rockets*, Vol. 40, No. 1, 2003, pp. 15–23.

[7] Pellegrino, S., "Deployable structures in engineering," *Deployable structures*, Springer, 2001, pp. 1–35.

[8] Carmi, M. O., Cooley, S., and Pellegrino, S., "Effects of Varying Geometric Design Parameters on the Stability of Deployable Thin-Shell Composite Space Structures," *AIAA SCITECH 2024 Forum*, 2024, p. 0606.

[9] Oberst, S., and Tuttle, S., "Nonlinear dynamics of thin-walled elastic structures for applications in space," *Mechanical Systems and Signal Processing*, Vol. 110, 2018, pp. 469–484.

[10] Guckenheimer, J., and Holmes, P., *Nonlinear oscillations, dynamical systems, and bifurcations of vector fields*, Vol. 42, Springer Science & Business Media, 2013.

[11] Murphey, T. W., and Banik, J., "Triangular rollable and collapsible boom," , 2011. USA Patent 7,895,795.

[12] Arya, M., Lee, N., and Pellegrino, S., "Ultralight structures for space solar power satellites," *3rd AIAA Spacecraft Structures Conference*, 2016, p. 1950.

[13] Bolotin, V., *The Dynamic Stability of Elastic Systems, Volume 1*, Aerospace Corporation, Systems Research and Planning Division, 1962.

[14] Majorana, C., and Pellegrino, C., "Dynamic stability of elastically constrained beams: an exact approach," *Engineering Computations*, Vol. 14, No. 7, 1997, pp. 792–805.

[15] Carrera, E., Cinefra, M., Petrolo, M., and Zappino, E., *Finite element analysis of structures through unified formulation*, John Wiley & Sons, Hoboken, New Jersey, USA, 2014.

[16] Carrera, E., Pagani, A., and Augello, R., "Evaluation of geometrically nonlinear effects due to large cross-sectional deformations of compact and shell-like structures," *Mechanics of Advanced Materials and Structures*, Vol. 27, No. 14, 2020, pp. 1269–1277.

[17] Augello, R., Carrera, E., Pagani, A., and Pellegrino, S., "Folding simulation of TRAC longerons via unified one-dimensional finite elements," *Materials Research Proceedings*, Vol. 37, 2024.

[18] Pagani, A., Augello, R., and Carrera, E., "Numerical simulation of deployable ultra-thin composite shell structures for space applications and comparison with experiments," *Mechanics of Advanced Materials and Structures*, Vol. 30, No. 8, 2023, pp. 1591–1603.

[19] Reddy, N. H., and Pellegrino, S., "Dynamics of the Caltech SSPP deployable structures: structure–mechanism interaction and deployment envelope," *AIAA Scitech 2023 Forum*, 2023, p. 2065.

[20] Leclerc, C., and Pellegrino, S., "Nonlinear elastic buckling of ultra-thin coilable booms," *International Journal of Solids and Structures*, Vol. 203, 2020, pp. 46–56.

[21] Feldman, M., *Hilbert transform applications in mechanical vibration*, John Wiley & Sons, 2011.

[22] Pagani, A., and Carrera, E., "Unified formulation of geometrically nonlinear refined beam theories," *Mechanics of Advanced Materials and Structures*, Vol. 25, No. 1, 2018, pp. 15–31.

[23] Hilber, H. M., Hughes, T. J., and Taylor, R. L., "Improved numerical dissipation for time integration algorithms in structural dynamics," *Earthquake Engineering & Structural Dynamics*, Vol. 5, No. 3, 1977, pp. 283–292.

[24] Azzara, R., Filippi, M., and Pagani, A., "Variable-kinematic finite beam elements for geometrically nonlinear dynamic analyses," *Mechanics of Advanced Materials and Structures*, Vol. 30, No. 20, 2023, pp. 4146–4154.

[25] Carrera, E., Pagani, A., Augello, R., and Wu, B., "Popular benchmarks of nonlinear shell analysis solved by 1D and 2D CUF-based finite elements," *Mechanics of Advanced Materials and Structures*, Vol. 27, No. 13, 2020, pp. 1098–1109.

[26] Pagani, A., Augello, R., and Carrera, E., "Frequency and mode change in the large deflection and post-buckling of compact and thin-walled beams," *Journal of Sound and Vibration*, Vol. 432, 2018, pp. 88–104.